Reconstructions of Chest Phantoms by the D-Bar Method for Electrical Impedance Tomography

David Isaacson, *Member, IEEE*, Jennifer L. Mueller*, Jonathan C. Newell, *Member, IEEE*, and Samuli Siltanen

***Abstract*—The problem this paper addresses is how to use the two-dimensional D-bar method for electrical impedance tomography with experimental data collected on finitely many electrodes covering a portion of the boundary of a body. This requires an approximation of the Dirichlet-to-Neumann, or voltage-to-current density map, defined on the entire boundary of the region, from a finite number of matrix elements of the current-to-voltage map. Reconstructions from experimental data collected on a saline filled tank containing agar heart and lung phantoms are presented, and the results are compared to reconstructions by the NOSER algorithm on the same data.**

***Index Terms*—D-bar method, direct reconstruction algorithm, electrical impedance tomography.**

I. Introduction

ELECTRICAL impedance tomography (EIT) is a relatively new imaging modality in which electrodes are placed on the surface of the body and the conductivity in the interior of the body is reconstructed from voltage data arising from currents applied on the electrodes. Since the various tissues and organs in the body often have different conductivities, an image is created from the reconstruction. Often, these electrodes are placed around the circumference of the thorax, and a cross-sectional image is formed from a two-dimensional (2-D) reconstruction. In this geometry, clinical applications include monitoring heart and lung function, diagnosis of pulmonary embolus, and diagnosis of pulmonary edema.

The problem is modeled by the conductivity equation

$$\nabla \cdot (\gamma(x,y)\nabla u(x,y)) = 0, \quad (x,y) \in \Omega \tag{1}$$

where Ω denotes a 2-D simply connected domain, γ denotes the conductivity of the body and u the electric potential. Applying a known voltage f on the boundary of Ω corresponds to the Dirichlet boundary condition

$$u(x,y) = f(x,y), \quad (x,y) \in \partial\Omega \tag{2}$$

Manuscript received November 21, 2003; revised February 27, 2004. This work was supported in part by the Center for Subsurface Sensing and Imaging Systems (Cen SSIS) throught the Engineering Research Centers Program of the National Science Foundation (NSF) under Award EEC-998621. The work of J. L. Mueller was supported in part by the National Science Foundation under Grant DMS-0104861. The Associate Editor responsible for coordinating the review of this paper and recommending its publication was C. Crawford. *Asterisk indicates corresponding author.*

D. Isaacson and J. C. Newell are with Rensselaer Polytechnic Institute, Troy, NY 12180 USA.

*J. L. Mueller is with Colorado State University, Fort Collins, CO 80523 USA (e-mail: mueller@math.coloradostate.edu).

S. Siltanen is with Instrumentarium Corporation, Imaging Division, FIN-04301 Tuusula, Finland.

Digital Object Identifier 10.1109/TMI.2004.827482

where $\partial\Omega$ denotes the boundary of Ω. Measuring the resulting current density distribution j on the boundary corresponds to knowing the Neumann boundary condition

$$\gamma(x,y)\frac{\partial u}{\partial \nu}(x,y) = j(x,y) \tag{3}$$

where ν denotes the outward normal to $\partial\Omega$. The mapping which takes a given voltage distribution on the boundary to the resulting current density distribution on the boundary is referred to as the Dirichlet-to-Neumann, or voltage-to-current density, map and is denoted by Λ_γ. Thus, $\Lambda_\gamma f = j$.

The uniqueness question for the inverse conductivity problem is whether the Dirichlet-to-Neumann map uniquely determines the conductivity $\gamma(x,y)$. That is, does $\Lambda_{\gamma_1} = \Lambda_{\gamma_2}$ imply $\gamma_1 = \gamma_2$? The reconstruction problem is how to determine $\gamma(x,y)$ from knowledge of the Dirichlet-to-Neumann map. For a survey of results on the uniqueness question under various assumptions on γ and $\partial\Omega$ and for a brief survey of reconstruction algorithms, see, for example, [35] or [11] and the references therein. The uniqueness question for a bounded domain in R^2 for sufficiently regular conductivities having essentially two derivatives was first solved by Nachman [37] in 1996, for less regular conductivities with only one derivative by Brown and Uhlmann [16] in 1997, and for L^∞ conductivities by Astala and Päivärinta [3] in 2003. The proof [37] uses the D-bar method of inverse scattering and outlines a direct reconstruction method for the conductivity. In a series of papers [43], [45], [35], [36], the authors presented a numerical method for solving the equations in Nachman's proof and applied the method to numerically simulated data.

This paper addresses the problem of how to approximate the Dirichlet-to-Neumann map Λ_γ defined on the entire boundary of $\partial\Omega$ from measurements made only on a portion of the boundary. In previous publications by the authors, the Dirichlet-to-Neumann map was known. However, in this paper, we approximate the voltage-to-current density operator Λ_γ from a finite number of discrete measured matrix elements of the current-to-voltage mapping. To model the current density on the electrodes, the gap model [48] is employed, and a matrix representation of the Dirichlet-to-Neumann map is derived. This is the first paper using the D-bar method to use the gap model; previous works used the continuum model since Λ_γ was known. We derive an approximation to the scattering transform used in the D-bar method in terms of the discrete current-to-voltage matrix. The algorithm is then used to reconstruct the conductivity distribution inside a phantom chest consisting of agar heart and lungs in a saline bath from

current-to-voltage data measured on 32 electrodes on the boundary of the tank.

The results from the reconstruction are compared to the NOSER algorithm [19], [46]. NOSER, named for Newton's One-Step Error Reconstructor, is a linearization-based algorithm which takes one step of Newton's Method, using the best constant conductivity approximation from the measured data as an initial guess. Other examples of linearization-based algorithms include backprojection methods [6], [12], [42], Calderón's approach [17], [18], [27] moment methods [2], and other one-step Newton methods [13], [33], [34]. Algorithms that solve the full nonlinear problem include approaches based on output least-squares [14], [15], [20]–[22], [29], [30], [53], the equation-error formulation [31], [32], [52], statistical inversion [28], and layer stripping [47], [51].

This paper is organized as follows. In Section II, we describe the steps of the reconstruction algorithm. Descriptions of the implementation of the algorithm are provided in [35], [36], [43], [45]. Section III contains a description of the electrode model as well as definitions of the operators and matrices used in the derivation of the matrix approximation to the Dirichlet-to-Neumann map. The derivation of the discrete finite approximation to the Dirichlet-to-Neumann map is found in Section IV in which we also derive an approximation to the scattering transform in terms of this matrix. A brief description of the numerical solution of the D-bar equation is also found in Section IV. Section V contains the reconstructions of the phantom chest as well as comparisons to reconstructions by the NOSER algorithm.

II. The Reconstruction Algorithm

Nachman's uniqueness proof [37] for the 2-D inverse conductivity problem outlines a direct procedure for reconstructing the conductivity from knowledge of the Dirichlet-to-Neumann map. It is necessary to briefly outline the steps of the proof to fix notation for the remainder of the paper. For a more complete description of the method, the reader is referred to the original proof or to [35] or [43]. For an overview of the D-bar method applied to inverse scattering problems, the reader is referred to [7]. A selection of further references on inverse scattering and the D-bar method include [1], [8]–[10], [25], and [38]–[41].

The first step of the proof is to transform the conductivity (1) to the Schrödinger equation via the change of variables $q = \gamma^{-1/2}\Delta\gamma^{1/2}$ and $\tilde{u} = \gamma^{1/2}u$. Then

$$(-\Delta + q)\tilde{u} = 0 \quad \text{in } \Omega. \tag{4}$$

Under the assumption that $\gamma = 1$ near the boundary of the region Ω, one can smoothly extend $\gamma = 1$ and $q = 0$ to the whole plane $\mathbb{R}^2$. Let the variable z denote a point $z = (x, y) \in \mathbb{R}^2$, which will also be identified with a point in the complex plane by writing $z = x + iy$, where i denotes the complex number $\sqrt{-1}$. If $q = 0$, the function $\tilde{u} = e^{ikz} = e^{i(k_1+ik_2)(x+iy)}$ satisfies $-\Delta\tilde{u} = 0$ in $\mathbb{R}^2$ where k is a complex parameter $k \in \mathbb{C} \setminus 0$. This motivates the use of the Faddeev exponentially growing solutions solutions to the Schrödinger equation in the plane [24]. Nachman shows that the Faddeev solutions $\psi(z, k)$ are the unique solutions to the Schrödinger equation

$$(-\Delta + q)\psi(z, k) = 0 \quad z \in \mathbb{R}^2, \quad k \in \mathbb{C} \setminus 0 \tag{5}$$

for potentials q given by $q = \gamma^{-1/2}\Delta\gamma^{1/2}$ and $k \in \mathbb{C} \setminus 0$. Note that $\psi(z, k)$ is asymptotic to e^{ikz}. That is, for large $|z|$ or large $|k|$, $\psi(z, k)$ is approximately equal to e^{ikz} in a certain function space. Next, define the functions $\mu(z, k)$ by

$$\mu(z, k) := e^{-ikz}\psi(z, k).$$

The function μ satisfies an integral equation analogous to the classical Lippmann-Schwinger equation, and applying the operator $(\partial/\partial\bar{k}) = (1/2)((\partial)/(\partial k_1) + i(\partial)/(\partial k_2))$ to that equation yields the $\bar{\partial}$ equation

$$\frac{\partial}{\partial\bar{k}}\mu(z, k) = \frac{1}{4\pi\bar{k}}\mathbf{t}(k)e_{-k}(z)\overline{\mu(z, k)}, \qquad k \in \mathbb{C} \setminus 0, \quad z \in \mathbb{R}^2 \tag{6}$$

where the functions $e_k(z)$ and $\mathbf{t}(k)$ are defined by

$$\begin{aligned} e_k(z) &:= e^{2i(k_1x - k_2y)} \\ \mathbf{t}(k) &:= \int_{\mathbb{R}^2} e_k(z)q(z)\mu(z, k)dxdy \\ z &= (x, y) \in \mathbb{R}^2. \end{aligned} \tag{7}$$

Note that $|e_k(z)| = 1$. Nachman shows that the solution of the $\bar{\partial}$ equation (6) satisfies the weakly singular Fredholm integral equation of the second kind

$$\mu(z, s) = 1 + \frac{1}{(2\pi)^2}\int_{\mathbb{R}^2}\frac{\mathbf{t}(k)}{(s - k)\bar{k}} \times e_{-z}(k)\overline{\mu(z, k)}dk_1dk_2 \tag{8}$$

for all $k \in \mathbb{C} \setminus 0$. This formulation is used in the computations of $\mu(z, k)$.

Taking the small k limit of $\mu(z, k)$ gives the conductivity directly at each point z in Ω via the formula

$$\lim_{k\to 0}\mu(z, k) = \gamma^{1/2}(z), \quad z \in \Omega. \tag{9}$$

However, computations of $\mu(z, k)$ require knowledge of the function $\mathbf{t}(k)$, which is known as the scattering transform of q, and is not directly measurable in experiments. In the proof, Nachman shows that $\mathbf{t}(k)$ is related to the voltage-to-current data via the following integral equation on the boundary of $\Omega, \partial\Omega$:

$$\mathbf{t}(k) = \int_{\partial\Omega} e^{i\bar{k}\bar{z}}(\Lambda_\gamma - \Lambda_1)\psi(z, k)d\sigma(z). \tag{10}$$

Here, Λ_γ denotes the voltage-to-current density map when Ω contains the conductivity distribution $\gamma(z)$, Λ_1 denotes the voltage-to-current map when Ω contains a constant conductivity of 1, and $d\sigma(z)$ denotes the measure of arclength on $\partial\Omega$. Another integral equation relates the function $\psi(z, k)$ on $\partial\Omega$ to the difference of the voltage-to-current maps Λ_γ and Λ_1, but is omitted here since it is not used in this implementation.

We summarize the main steps of the algorithm as follows.

1) Find the solution to (5) $\psi|_{\partial\Omega}$ from the voltage-to-current map Λ_γ such that $\psi \sim e^{ikz}$ for large $|k|$.
2) Determine the scattering transform $\mathbf{t}$ from the voltage-to-current density map using (10).
3) Solve the D-bar equation (6) for $\mu(z,k)$ for $z \in \Omega, k \in \mathbb{C} \setminus 0$.
4) Reconstruct γ at each point $z \in \Omega$ from the formula (9).

In this section we relied on the assumption that $\gamma = 1$ in a neighborhood of the boundary of Ω. In practice, this assumption is necessarily violated by the presence of the electrodes on the boundary of the tank. Although the algorithm outlined in Nachman's proof contains an initial step in which the conductivity is reconstructed on $\partial\Omega$ and smoothly extended to 1 on the boundary of a slightly larger domain Ω_2 for which a new Dirichlet-to-Neumann map is then calculated, we omit that step in this work. Instead, we compute γ_{best}, the best constant conductivity approximation to γ from the measured data (see Appendix 1), and scale γ by γ_{best} so that

$$\tilde{\gamma} \equiv \gamma/\gamma_{\text{best}}. \tag{11}$$

Since $\Lambda_{c\gamma} = c\Lambda_\gamma$ for c constant, $\Lambda_{\tilde{\gamma}} = (1)/(\gamma_{\text{best}})\Lambda_\gamma$. Thus, we use the map $\Lambda_{\tilde{\gamma}}$ as our data corresponding to the scaled conductivity $\tilde{\gamma}$. After reconstructing $\tilde{\gamma}$, we obtain γ from the formula $\gamma = \gamma_{\text{best}}\tilde{\gamma}$. In the following sections we will simply use the notation γ to represent the scaled conductivity from (11) to avoid cumbersome notation.

III. The Experimental Configuration

Our experimental chest phantom consists of a circular tank with 32 equally spaced electrodes. See Fig. 1 for an illustration of the experimental configuration. In the following we will designate the number of electrodes by L and the radius of the tank by r. Let Ω denote the circle of radius 1 and Ω_r the circle of radius r. Let A denote the area of an electrode. The lth electrode is centered at angle $\theta_l = 2\pi l/L$. (Here, $L = 32$).

In practice, a basis of $L-1$ current patterns was applied on the L electrodes and the resulting voltages on the electrodes were measured. Although the algorithm requires an approximation to the voltage-to-current density map Λ_γ, it is desirable to apply currents because the current density-to-voltage map damps errors and noise in the data, while the voltage-to-current density map amplifies such errors. In this experiment, trigonometric current patterns were applied on the electrodes. These particular current patterns maximize the distinguishability as defined in [26] on the electrodes for a homogeneous medium, and were chosen for their ease of use. Note that the current density patterns that maximize the signal-to-noise ratio for any given conductivity distribution can be determined, as they are the eigenfunctions of the Dirichlet-to-Neumann map [26]. Let T^k denote the kth current pattern applied where

$$T_l^k = \begin{cases} M\cos(k\theta_l), & k=1,\ldots,\frac{L}{2}-1 \\ M\cos(\pi l), & k=L/2 \\ M\sin((k-L/2)\theta_l), & k=\frac{L}{2}+1,\ldots,L-1 \end{cases} \tag{12}$$

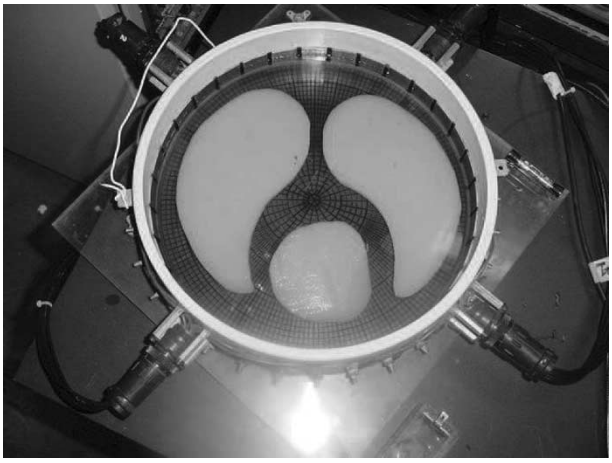

Fig. 1. The phantom chest.

and M is the current amplitude. Let V_l^k denote the voltage measured on the lth electrode corresponding to the kth current pattern T^k and normalized so that $\sum_{l=1}^{L} V_l^k = 0, k = 1,\ldots,L-1$. Let t^k denote the normalized currents $t^k = (T^k)/(\|T^k\|_2)$ and v^k the normalized voltages $v^k = (V^k)/(\|T^k\|_2)$, where $\|T^k\|_2 = \sqrt{\sum_{l=1}^{L}(T_l^k)^2}$. Let

- $\Lambda_{\gamma,r}$ denote the voltage-to-current density operator corresponding to a (scaled) conductivity distribution $\gamma(x)$ in a disk of radius r. (Note that $\Lambda_{1,1}$ then denotes the map corresponding to a conductivity of 1 in a disk of radius 1.)
- $R_{\gamma,r}$ denote the current density-to-voltage operator corresponding to a (scaled) conductivity distribution $\gamma(x)$ in a disk of radius r. (Note that $R_{\gamma,r} = \Lambda_{\gamma,r}^{-1}$.)

We model the current density $j(x,y)$ on the boundary by the gap model so that

$$j(x,y) = \begin{cases} \frac{I_l}{A_l}, & (x,y) \in e_l \\ 0, & \text{otherwise} \end{cases}$$

where I_l is the current applied on the lth electrode, e_l denotes the lth electrode and A_l is the area of the lth electrode.

We denote the current-to-voltage matrix by $R_{\gamma,r}^M$. An entry of $R_{\gamma,r}^M$ is defined by $R_{\gamma,r}^M(m,n) = (t_l^m, v_l^n)_L$. Let $\tilde{R}_{\gamma,r}^M$ be the matrix defined by $\tilde{R}_{\gamma,r}^M(m,n) = ((t_l^m)/(A), v_l^n)_L$ where the vectors t^m and v^n of length L are defined in Section 4 and A is the area of an electrode. (All of the electrodes have the same area.) Then $A\tilde{R}_{\gamma,r}^M = R_{\gamma,r}^M$. Let $\mathbf{L}_{\gamma,r} \equiv (\tilde{R}_{\gamma,r}^M)^{-1}$. Then the entries of $\mathbf{L}_{\gamma,r}$ are the elements of the discrete voltage-to-current map. Let $R_{1,r}^M$, $\tilde{R}_{1,r}^M$, and $\mathbf{L}_{1,r}$ be defined analogously. The matrix $\delta\mathbf{L} \equiv \mathbf{L}_{\gamma,r} - \mathbf{L}_{1,r}$ is the discrete voltage-to-current map that will serve as the approximation to $\Lambda_\gamma - \Lambda_1$ in the algorithm. It is used explicitly in the construction of the scattering transform $\mathbf{t}(k)$. The relationship between $\Lambda_\gamma - \Lambda_1$ and $\delta\mathbf{L}$ is derived in Section IV.B.

IV. Numerical Techniques

In this section we describe the numerical techniques used to reconstruct the conductivity γ given by (11) using the D-bar method and experimental data.

A. Approximating Ψ on the Boundary

The first step of the reconstruction is to compute the exponentially growing solution ψ to (5) on the boundary $\partial\Omega$ of Ω. A Fredholm integral equation for computing ψ on $\partial\Omega$ from the Dirichlet-to-Neumann map is given in [37]. While this equation is theoretically solvable, the operator which must be inverted to solve the equation may no longer be invertible when there is noise in the Dirichlet-to-Neumann map. The regularization of this operator is a subject of future research. Instead, we approximate ψ on $\partial\Omega$ by its asymptotic behavior e^{ikz} and set $\psi(z,k) := e^{ikz}$ on $\partial\Omega$. This approximation was first introduced in [43] and was further studied in [35]. The effects of this approximation remain unknown.

B. Approximating the Scattering Transform $\mathbf{t}(k)$

In this section we derive the approximation $\mathbf{t}^{\exp}$ to the scattering transform from experimental data to the theoretical scattering transform $\mathbf{t}(k)$. Since the formula for $\mathbf{t}(k)$ given in (10) is valid for the Dirichlet-to-Neumann map defined on the boundary of the unit disk, we must derive an approximation $\mathbf{t}^{\exp}$ on a disk of radius r using the matrix approximation to Λ_γ corresponding to current-to-voltage data measured on L electrodes.

Substituting the approximation $\psi(z,k) := e^{ikz}$ on $\partial\Omega$ into (10) and denoting our approximation by $\mathbf{t}^{\exp}$ gives

$$\mathbf{t}^{\exp}(k) = \int_{\partial\Omega} e^{i\bar{k}\bar{z}}(\Lambda_{\gamma,1} - \Lambda_{1,1})e^{ikz}d\sigma(z). \tag{13}$$

As in [43], we expand e^{ikz} in a Fourier series with $z = e^{i\theta}$ to obtain

$$e^{ikz} = \sum_{n=-\infty}^{\infty} a_n(k)e^{in\theta} \quad \text{with}$$
$$a_n(k) = \begin{cases} \frac{(ik)^n}{n!}, & n \geq 0 \\ 0, & n < 0 \end{cases}.$$

Define the inner product $\langle f, g\rangle$ by

$$\langle f, g\rangle = \int_0^{2\pi} \overline{f(\theta)}g(\theta)d\theta.$$

Then, substituting the series for e^{ikz} into (13) gives

$$\mathbf{t}^{\exp}(k) = \sum_{m=0}^{\infty}\sum_{n=0}^{\infty} a_m(\bar{k})a_n(k) \times \langle e^{im\theta}, (\Lambda_{\gamma,1} - \Lambda_{1,1})e^{in\cdot}(\theta)\rangle. \tag{14}$$

Note that (14) holds on the unit disk while our data is measured on a disk of radius r. Since $\Lambda_{\gamma,1} = r\Lambda_{\gamma,r}$, (14) becomes

$$\mathbf{t}^{\exp}(k) = r\sum_{m=0}^{\infty}\sum_{n=0}^{\infty} a_m(\bar{k})a_n(k) \times \langle e^{im\theta}, (\Lambda_{\gamma,r} - \Lambda_{1,r})e^{in\cdot}(\theta)\rangle. \tag{15}$$

For functions u, w of $\theta, u, w : \mathbb{R}^l \to \mathbb{R}$, let $(u(\cdot), w(\cdot))_L$ denote the discrete inner product defined by

$$(u(\cdot), w(\cdot))_L = \sum_{l=1}^{n} \overline{u(\theta_l)}w(\theta_l).$$

Since $\Lambda_{\gamma,r} = R_{\gamma,r}^{-1}$, we have that

$$\begin{aligned}\langle e^{im\theta}, \Lambda_{\gamma,r}(e^{in\cdot})(\theta)\rangle &= \frac{1}{A}\langle e^{im\theta}, A\Lambda_{\gamma,r}(e^{in\cdot})(\theta)\rangle \\ &= \frac{1}{A}\left\langle e^{im\theta}, AR_{\gamma,r}^{-1}(e^{in\cdot})(\theta)\right\rangle \\ &= \frac{1}{A}\left\langle e^{im\theta}, \left(\frac{R_{\gamma,r}}{A}\right)^{-1}(e^{in\cdot})(\theta)\right\rangle.\end{aligned}$$

Applying the gap model for the current density on the electrodes gives an approximation in terms of the discrete inner product

$$\begin{aligned}&\frac{1}{A}\left\langle e^{im\theta}, \left(\frac{R_{\gamma,r}}{A}\right)^{-1}(e^{in\cdot})(\theta)\right\rangle \\ &\quad\approx \frac{\Delta\theta}{A}\left(e^{im\cdot}, \left(\frac{R_{\gamma,r}}{A}\right)^{-1}(e^{in\cdot})\right)_L\end{aligned}$$

where $\Delta\theta = 2\pi/L$. Thus

$$\langle e^{im\theta}, \Lambda_{\gamma,r}(e^{in\cdot})(\theta)\rangle \approx \frac{\Delta\theta}{A}\left(e^{im\cdot}, \left(\frac{R_{\gamma,r}}{A}\right)^{-1}(e^{in\cdot})\right)_L. \tag{16}$$

Using Euler's formula $e^{in\theta_l} = \cos n\theta_l + i\sin n\theta_l$ gives

$$\begin{aligned}&\left(e^{im\cdot}, \left(\frac{R_{\gamma,r}}{A}\right)^{-1}(e^{in\cdot})\right)_L \\ &\quad= \left(\cos m\cdot, \left(\frac{R_{\gamma,r}}{A}\right)^{-1}(\cos n\cdot)\right)_L \\ &\qquad+ i\left(\cos m\cdot, \left(\frac{R_{\gamma,r}}{A}\right)^{-1}(\sin n\cdot)\right)_L \\ &\qquad- i\left(\sin m\cdot, \left(\frac{R_{\gamma,r}}{A}\right)^{-1}(\cos n\cdot)\right)_L \\ &\qquad+ \left(\sin m\cdot, \left(\frac{R_{\gamma,r}}{A}\right)^{-1}(\sin n\cdot)\right)_L.\end{aligned} \tag{17}$$

Consider the first term in the sum (17). From (12)

$$\begin{aligned}&\left(\cos m\cdot, \left(\frac{R_{\gamma,r}}{A}\right)^{-1}(\cos n\cdot)\right)_L \\ &\quad= \frac{\|T^m\|_2\|T^n\|_2}{M^2}\left(t_l^m, \left(\frac{R_{\gamma,r}}{A}\right)^{-1}t_l^n\right)_L \\ &\quad\approx \frac{\|T^m\|_2\|T^n\|_2}{M^2}\left(\tilde{R}_{\gamma,r}^M\right)^{-1}(m,n) \\ &\quad= \frac{\|T^m\|_2\|T^n\|_2}{M^2}\mathbf{L}_{\gamma,\mathbf{r}}(m,n).\end{aligned} \tag{18}$$

Note that

$$||T^n||_2 = \begin{cases} M\sqrt{L/2}, & n \neq L/2 \\ M\sqrt{L}, & n = L/2 \end{cases}.$$

Let $\delta\mathbf{L}_{m,n} \equiv \mathbf{L}_{\gamma,r}(m,n) - \mathbf{L}_{1,r}(m,n)$. Then from (15), (16), and (18)

$$\begin{aligned}\mathbf{t}^{\exp}(k) \approx \frac{Lr\Delta\theta}{2A}\Bigg(&\sum_{m=1}^{L/2-1}\sum_{n=1}^{L/2-1} a_m(\bar{k})a_n(k)\Big(\delta\mathbf{L}_{m,n} \\ &+ \delta\mathbf{L}_{\frac{L}{2}+m,\frac{L}{2}+n} + i\Big(\delta\mathbf{L}_{m,\frac{L}{2}+n} - \delta\mathbf{L}_{\frac{L}{2}+m,n}\Big)\Big) \\ &+ \sqrt{2}\sum_{n=1}^{\frac{L}{2}-1} a_{\frac{L}{2}}(\bar{k})a_n(k)\Big(\delta\mathbf{L}_{\frac{L}{2},n} + i\delta\mathbf{L}_{\frac{L}{2},\frac{L}{2}+n}\Big) \\ &+ \sqrt{2}\sum_{m=1}^{\frac{L}{2}-1} a_m(\bar{k})a_{\frac{L}{2}}(k)\Big(\delta\mathbf{L}_{m,\frac{L}{2}} \\ &- i\ \delta\mathbf{L}_{\frac{L}{2}+m,\frac{L}{2}}\Big) + 2a_{\frac{L}{2}}(\bar{k})a_{\frac{L}{2}}(k)\Big(\delta\mathbf{L}_{\frac{L}{2},\frac{L}{2}}\Big)\Bigg).\end{aligned}$$

To approximate the matrix $\mathbf{L}_{1,r}$, note that for $m, n \leq L/2$

$$\begin{aligned}\mathbf{L}_{1,r}(m,n) &= \left(\tilde{R}^M_{1,r}\right)^{-1}(m,n) \\ &\approx \left(\frac{M\cos m\cdot}{||T^m||_2}, \left(\frac{R_{1,r}}{A}\right)^{-1}\left[\frac{M\cos n\cdot}{||T^n||_2}\right]\right)_L \\ &= \frac{M^2}{||T^m||_2||T^n||_2}\left(\cos m\cdot, \left(\frac{R_{1,r}}{A}\right)^{-1}[\cos n\cdot]\right)_L \\ &= \frac{M^2A}{||T^m||_2||T^n||_2}\left(\cos m\cdot, R^{-1}_{1,r}[\cos n\cdot]\right)_L \\ &= \frac{M^2A}{||T^m||_2||T^n||_2}(\cos m\cdot, \Lambda_{1,r}[\cos n\cdot])_L \\ &= \frac{A}{r}\left(\frac{M\cos m\cdot}{||T^m||_2}, \Lambda_{1,1}\left[\frac{M\cos n\cdot}{||T^n||_2}\right]\right)_L.\end{aligned}$$

Since $\Lambda_{1,1}[(M\cos n\theta_l/||T^n||_2)] = |n|(M\cos n\theta_l)/(||T^n||_2)$, the matrix $\mathbf{L}_{1,r}$ is approximated by the diagonal matrix

$$\mathbf{L}_{1,r}(m,n) = \frac{A}{r}\begin{cases} m, & m = n \text{ and } m, \quad n \leq L/2 \\ m - L/2, & m = n \text{ and } m, \quad n > L/2 \\ 0, & \text{otherwise.} \end{cases}$$

C. Numerical Solution of the $\bar{\partial}$ Equation

The solution $\mu(x,k)$ to the D-bar equation (6) is found by solving the integral (8) for all $k \in \mathbb{C}\setminus 0$ and for each $z \in \Omega$. It is shown in [43] that for sufficiently smooth conductivities, $\mathbf{t}(k)/\bar{k}$ is bounded at $k = 0$ and the integrand in (8) approaches zero as $|k| \to \infty$. Thus, the integral over $\mathbb{R}^2$ can be approximated by an integral over a square $[-A, A]^2$ on a uniform mesh consisting of N^2 square elements, chosen in such a way that $k = 0$ is not on a corner of a mesh element. Thus, the mesh is determined by A and N, and the length of a side of a mesh element is given by $h = 2A/(N+1)$. Note that the function $\mu(x,k)$ is oscillatory in both x and k, and the k grid should be sufficiently fine to capture these oscillations. We solve (8) numerically using a 2-D adaptation of the method of product integrals presented in [4]. The idea of the method is to factor the integrand into its smooth part and its singular part and approximate the smooth part with a simple function, such as an interpolatory polynomial. The new integrand is then computed analytically where possible. See the [35] or [36] for a detailed description of the implementation.

The method results in a system of the form

$$\mathbf{I}\mu(z) - \mathbf{A}\bar{\mu}(z) = \mathbf{g}(z) \tag{19}$$

where $\mathbf{I}$ and $\mathbf{A}$ are matrices of size N^2 by N^2. This type of system is known as $\mathbb{R}$-linear and can be solved by equating the real and imaginary parts to obtain a linear system of size $2N^2$ by $2N^2$ in real variables with two vectors of unknowns $\Re\mu$ and $\Im\mu$. In this implementation the system was solved using LU decomposition with partial pivoting and row exchanges, so the computational complexity of the method is $O(8N^6/3)$.

The system must be solved for each $z \in \Omega$. However, in practice Ω is discretized into M mesh elements, the conductivity is assumed to be a constant γ_j in the jth mesh element, and the equation is solved for a specified z_j in mesh element j. The solution of the system (19) results in a set of values of $\mu(z_j,k)$ on a k-mesh in $\mathbb{C}$. Recall that the conductivity is given by

$$\gamma^{1/2}(z) = \lim_{k\to 0}\mu(z,k). \tag{20}$$

The value of $\mu(z_j,0)$ was approximated in this implementation using bicubic interpolation on the 16 values of $\mu(z_j,k)$ nearest $k = 0$ in the k-mesh.

This method of solving (8) described above and in further detail in [35] has the advantage that certain factors in the matrix $\mathbf{A}$ are independent of z, so they need only be computed once and stored. Thus, the factors are computed, and then the system is solved for each z_j in parallel. Since these computations are independent, no communication is needed in the parallel implementation.

V. Reconstructions of Chest Phantoms

The algorithm was tested on experimental data collected on a phantom chest which consisted of agar heart and lungs in a saline bath in a tank of radius 15 cm with 32 electrodes of size 1.6 cm high and 2.5 cm wide. The conductivity of the saline was 424 mS/m, the conductivity of the agar lungs was 240 mS/m, and the conductivity of the agar heart was 750 mS/m. A photo of the configuration is found in Fig. 1. The data was collected using the ACT3 system [23] at Rensselaer Polytechnic Institute. ACT 3 is a 32-electrode system operating at 28.8 kHz that applies currents and measures the real and quadrature components of the voltage on all 32 electrodes simultaneously.

In this experiment the trigonometric current patterns given in Section III were applied with an amplitude of .2 mA on the 32 electrodes and the resulting voltage was measured. The voltage-to-current map $\mathbf{L}_{\gamma,r}$ was constructed by the method described in Section III.

The numerical approximation to the scattering transform $\mathbf{t}(k)$ was computed by the method in Section IV.B. The approximate $\mathbf{t}^{\exp}$ "blew up" exponentially fast as $|k|$ increased, that is, $\lim_{|k|\to\infty}|\mathbf{t}^{\exp}(k)| = \infty$, due to the fact that the compuational

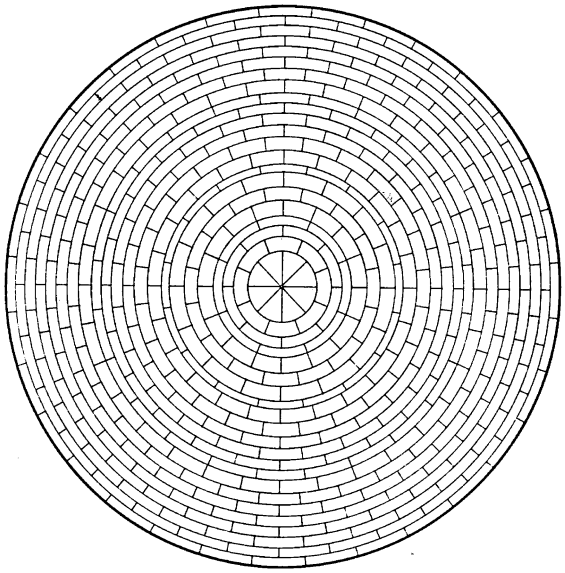

Fig. 2. The 496-element "Joshua tree" mesh.

$\mathbf{t}^{\exp}$ is a polynomial approximation to an infinite power series and there is noise in the coefficients. The approximation was regularized by truncating $\mathbf{t}^{\exp}(k)$ to 0 outside a circle of radius R in the k-plane. This regularization was studied in [35] where noisy simulated data also led to blow up in $\mathbf{t}^{\exp}$. Also in [35] is a study of the effects of truncating the actual scattering transform $\mathbf{t}(k)$ at radius R on the reconstructions, and it is shown that the reconstructions corresponding to such truncations will converge, as $R \to \infty$, to the correct conductivity, and several numerical examples are provided. In this paper, the truncation radius R was chosen by inspection of the scattering transform and the reconstructed conductivity. It was found that as R increased, oscillations appeared in the reconstructed conductivity with an unacceptable level of oscillation occuring with $R = 4$. The results here correspond to $R = 3.5$, which resulted in a reasonably flat image for the interior of the homogeneous tank. We do not address the question of how to choose R without using this kind of *a priori* information in this work.

The reconstructed conductivity was obtained by solving the $\bar{\partial}$ equation by the method of Section IV.C on the rectangle $[-3.5, 3.5]^2$ in the complex k-plane with $N = 38$ (hence mesh elements of size .1795 by .1795) and on the NOSER, or "Joshua tree," mesh in the x-variable. See Fig. 2 for an illustration of the mesh. This mesh contains 496 elements, the maximum number of degrees of freedom for reconstructing the conductivity from 31 current patterns on 32 electrodes $(L(L-1)/2)$. There are 32 elements on the outermost and several adjacent layers. All mesh elements have the same area and can be specified by radial and angular subdivisions. The Joshua tree mesh was introduced in [19], to which the reader is referred for further discussion of the mesh design. The conductivity is chosen to be constant in each mesh element with z_j defined to be the radial and angular center of the jth element. The reconstructions were then plotted using the ACT3 display system which includes a low-pass filter. Reconstructions from the same data sets were also computed using the NOSER algorithm [19].

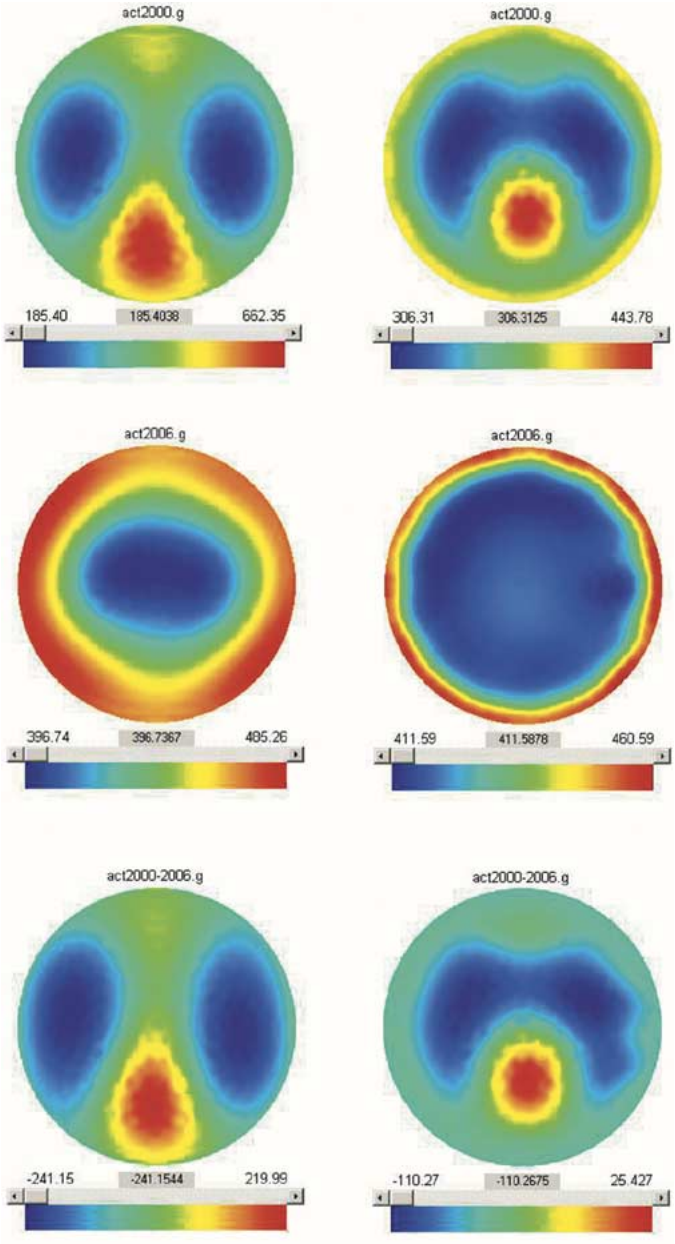

Fig. 3. Top row: Static reconstructions of the phantom chest using the D-bar method (left) and NOSER (right). Second row: Static reconstructions of the homogeneous tank using the D-bar method (left) and NOSER (right). Bottom row: Difference images using D-bar (left) and NOSER (right).

NOSER, named for Newton's One-Step Error Reconstructor, is a linearization-based algorithm which takes one step of Newton's Method, using the constant conductivity γ_{best} as an initial guess. For more details on NOSER, see the [19] or [46]. The same value for γ_{best} was used in the D-bar images as in the NOSER images. For the homogeneous tank $\gamma_{\text{best}} = 430$ mS/m and for the phantom chest $\gamma_{\text{best}} = 363$ mS/m.

Static reconstructions of the phantom chest and the homogeneous tank using the D-bar and NOSER algorithms are found in Fig. 3. Difference images formed by subtracting the reconstructed conductivities are also found in Fig. 3. In the static images, the reconstructed conductivity from the D-bar method has a maximum value of 662 mS/m, found in the heart region.

This constitutes a relative error of 12% for the heart region. The static NOSER images have a maximum of 444 mS/m, found in the heart region, which corresponds to a relative error of 41%. The reconstructed conductivity from the D-bar method has a minimum value of 185 mS/m, found in the lung region, which corresponds to a relative error of 23%, compared with a relative error of 28% from NOSER for the lung region. One sees from the static image of the homogeneous tank that the background conductivity of 424 mS/m for the saline was well-recovered in the NOSER images (to within 3% relative error). As is typical in NOSER images, the electrodes appear as a conductive ring around the boundary of the image. The D-bar image contains a much wider ring of high conductivity near the boundary, with a minimum conductivity of 397 mS/m in the interior, which is a relative error of 6.5% for the saline. The spatial resolutions of the static reconstructions of the phantom chest differ somewhat. The D-bar image recovers the separation between the two agar lungs, while the NOSER reconstruction does not, but the overall size and position of the lungs appears more accurate in the static NOSER image. There is also distortion of the agar heart in the D-bar image. In terms of dynamic range, the NOSER static image of the phantom chest has about 27% of the "truth" while the dynamic range of the D-bar static image is about 93% of the "truth" where "truth" is taken to be the difference between the agar conductivity of heart (750) and lungs $(240) = 510$.

Some artifacts in the D-bar images may be a result of the omission of the implementation of the very first step of the algorithm which requires reconstructing the conductivity on the boundary of the region, extending the conductivity outside the region to a larger region with a conductivity of 1 on its boundary and forming a new Dirichlet-to-Neumann map for this new domain. This step was not required in previous work since the data was numerically simulated. Implementation of this step is expected to improve the images and requires further research. Choosing a larger truncation radius R for $\mathbf{t}^{\exp}$ results in a smaller conductive ring near the boundary, but contains oscillations of high and low conductivity in the interior. Further improvements may come from a better representation of the scattering transform, which may be obtained by solving (10) for $\mathbf{t}(k)$ or using another type of approximation, such as the one developed in [35].

For the reader comparing the images in this work to those in [36], in which reconstructions of a numerically simulated phantom chest are published, we point out that only the accuracy of the solution of the D-bar equation was being tested in [36], since the scattering transform was computed from the definition which assumes prior knowledge of the conductivity (see [36] for details). Furthermore, the numerically simulated chest consisted of a smooth (C^2) conductivity distribution, while the distribution in this work is discontinuous. Studies of numerically simulated discontinuous conductivity distributions with noise in the data are a subject of future work. The practical value of the images presented here is that they demonstrate that this kind of regularization of the D-bar method works on experimental data and the reconstructions are reasonably accurate in terms of conductivity value and spatial information.

VI. Conclusion

In this paper, the D-bar method for electrical impedance tomography in the 2-D, cross-sectional geometry was further developed and used to reconstruct agar heart and lung phantoms in a saline-filled tank. The locations of the phantom heart and lungs were reasonably well represented in both the static reconstructions and the difference images. However, the reconstruction of the homogeneous tank exhibited a large artifact near the boundary due to the presence of the electrodes. The values of the reconstructed conductivity were within 23% of the actual values of the phantom chest, and the dynamic range of the reconstructed values was 93% of the actual range. These results were compared to reconstructions by the NOSER algorithm on the same data, which yielded conductivity values with a 41% relative error, and a dynamic range of only 27% of its actual values. The results demonstrate that the D-bar algorithm can be used to obtain useful images on measured data, but further refinements are needed to reduce artifacts.

Appendix I
Computing ρ_{best}

The best constant conductivity approximation to the measured voltage data can be computed according to the following formula. Let ρ denote the resistivity (the reciprocal of the conductivity γ.) Then for a homogeneous medium, the voltage on the lth electrode from the kth current pattern is proportional to the voltage arising from a constant distribution of one

$$V_l^k(\rho) = \rho V_l^k(1). \tag{21}$$

Let $\{U_l^k\}$ denote the set of measured voltage data and $V_l^k(\rho)$ the calculated voltage on the electrodes. To find the best fit to the data, we must solve

$$\min_{\rho} \sum_{k=1}^{K} \sum_{l=1}^{L} \left(\rho V_l^k(1) - U_l^k\right)^2. \tag{22}$$

The solution ρ_{best} to this minimization problem is given by

$$\rho_{\text{best}} = \frac{\sum_{k=1}^{K} \sum_{l=1}^{L} V_l^k(1) U_l^k}{\sum_{k=1}^{K} \sum_{l=1}^{L} V_l^k(1) V_l^k(1)}. \tag{23}$$

Acknowledgment

The authors thank G. Saulnier for his help with the data collection and the anonymous referees for their careful reading of the paper and constructive comments.

References

[1] M. J. Ablowitz, D. B. Yaacov, and A. S. Fokas, "On the inverse scattering transform for the Kadomtsev-Petviashvili equation," *Studies Appl. Math.*, vol. 69, pp. 135–143, 1983.

[2] A. Allers and F. Santosa, "Stability and resolution analysis of a linearized problem in electrical impedance tomography," *Inverse Problems*, vol. 7, pp. 515–533, 1991.

[3] K. Astala and L. Päivärinta, Calderón's Inverse Conductivity Problem in the Plane, 2003. preprint.

[4] K. Atkinson, *An Introduction to Numerical Analysis*, 2nd ed. New York: Wiley, 1989.

[5] D. C. Barber and B. H. Brown, "Applied potential tomography," *J. Phys. E. Sci. Instrum.*, vol. 17, pp. 723–733, 1984.

[6] ——, "Progress in electrical impedance tomography," in *Inverse Problems in Partial Differential Equations*. Philadelphia, PA, 1990.

[7] R. Beals and R. R. Coifman, "Linear spectral problems, nonlinear equations and the $\bar{\partial}$ method," *Inverse Problems*, vol. 5, pp. 87–130, 1989.

[8] ——, "Scattering, transformations spectrales et équations d'évolution non linéaire. I-II," presented at the Goulaouic-Meyer-Schwartz Seminar, 1981/1982, Exp. no. XXI, 9, 1982.

[9] ——, "Multidimensional Inverse Scattering and Nonlinear Partial Differential Equations," in *Proc. Symp Pure Mathematics*, vol. 43, 1985, pp. 45–70.

[10] ——, "The D-bar approach to inverse scattering and nonlinear evolution equations," *Physica*, vol. 18, pp. 242–249, 1986.

[11] L. Borcea, "Electrical impedance tomography," *Inverse Problems*, vol. 18, pp. 99–136, 2002.

[12] C. Berenstein and E. C. Tarabusi, "Inversion formulas for the k-dimensional Radon transform in real hyperbolic spaces," *Duke Math. J.*, vol. 62, pp. 1–19, 1991.

[13] R. Blue, "Real-time three-dimensional electrical impedance tomography," Ph.D. dissertation, RensselaerPolytech. Inst., Troy, NY, 1997.

[14] L. Borcea, "Nonlinear multigrid for imaging electrical conductivity and permittivity at low frequency," *Inverse Problems*, vol. 17, pp. 329–359, Apr. 2001.

[15] L. Borcea, J. G. Berryman, and G. Papanicolaou, "High contrast impedance tomography," *Inverse Problems*, vol. 12, pp. 835–858, 1996.

[16] R. M. Brown and G. Uhlmann, "Uniqueness in the inverse conductivity problem for nonsmooth conductivities in two dimensions," *Commun. Partial Differential Equations*, vol. 22, p. 1009, 1997.

[17] A. P. Calderón, "On an inverse boundary value problem," *Proc. Seminar Numerical Analysis and Its Applications to Continuum Physics*, pp. 65–73, 1980.

[18] M. Cheney, D. Isaacson, and E. L. Isaacson, "Exact solutions to a linearized inverse boundary value problem," *Inverse Problems*, vol. 6, pp. 923–934, 1990.

[19] M. Cheney, D. Isaacson, J. C. Newell, J. Goble, and S. Simske, "Noser: And algorithm for solving the inverse conductivity problem," *Int. J. Imag. Syst. Technol.*, vol. 2, pp. 66–75, 1990.

[20] D. C. Dobson, "Convergence of a reconstruction method for the inverse conductivity problem," in *SIAM J. Appl. Math.*, vol. 52, 1992, pp. 442–458.

[21] D. C. Dobson and F. Santosa, "An image-enhancement technique for electrical impedance tomography," *Inverse Problems*, vol. 10, pp. 317–334, 1994.

[22] O. Dorn, H. B. Aguirre, J. G. Berryman, and G. Papanicolaou, "A nonlinear inversion method for 3D-electromagnetic imaging using adjoint fields," *Inverse Problems*, vol. 15, pp. 1523–1558, 1999.

[23] P. Edic, G. J. Saulnier, J. C. Newell, and D. Isaacson, "A real-time electrical impedance tomograph," *IEEE Trans. Biomed. Eng.*, vol. 42, pp. 849–859, Sept. 1995.

[24] L. D. Faddeev, "Increasing solutions of the Schrödinger equation," *Sov. Phys. Dokl*, vol. 10, pp. 1033–1035, 1966.

[25] A. S. Fokas and M. J. Ablowitz, "The inverse scattering transform for multidimensional $2 + 1$ problems," *Nonlinear Phenomena, Lecture Notes in Physics*, 1984.

[26] D. Isaacson, "Distinguishability of conductivities by electric current computed tomography," *IEEE Trans. Med. Imag.*, vol. MI-5, pp. 91–95, 1986.

[27] D. Isaacson and M. Cheney, "Effects of measurement precision and finite numbers of electrodes on linear impedance imaging algorithms," in *SIAM J. Appl. Math.*, vol. 15, 1991, pp. 1705–1731.

[28] J. Kaipio, V. Kolehmainen, E. Somersalo, and M. Vauhkonen, "Statistical inversion and Monte Carlo sampling methods in electrical impedance tomography," *Inverse Problems*, vol. 16, pp. 1487–1522, 2000.

[29] J. S. Kallman and J. G. Berryman, "Weighted least-squares criteria for electrical impedance tomography," *IEEE Trans. Med. Imag.*, vol. 11, pp. 284–292, June 1992.

[30] M. Klibanov, A Newton-Kantorovich method for impedance computed tomography, , vol. 41, no. 1, pp. 85–101, 1999.

[31] R. V. Kohn and A. McKenney, "Numerical implementation of a variational method for electrical impedance imaging," *Inverse Problems*, vol. 9, pp. 389–414, 1990.

[32] R. V. Kohn and M. Vogelius, "Relaxation of a variational method for impedance computed tomography," *Commun. Pure Appl. Math.*, vol. 40, pp. 745–777, 1987.

[33] J. L. Mueller, D. Isaacson, and J. C. Newell, "A reconstruction algorithm for electrical impedance tomography data collected on rectangular electrode arrays," *IEEE Trans. Biomed. Engr.*, vol. 49, pp. 1379–1386, Nov. 1999.

[34] ——, "Reconstruction of conductivity changes due to ventilation and perfusion from EIT data collected on a rectangular electrode array," *Physiol. Meas.*, vol. 22, pp. 97–106, 2001.

[35] J. L. Mueller and S. Siltanen, "Direct reconstructions of conductivities from boundary measurements," *SIAM J. Sci. Comp.*, vol. 24, pp. 1232–1266, 2003.

[36] J. L. Mueller, S. Siltanen, and D. Isaacson, "A direct reconstruction algorithm for electrical impedance tomography," *IEEE Trans. Med. Imag.*, vol. 21, pp. 555–559, June 2002.

[37] A. I. Nachman, "Global uniqueness for a two-dimensional inverse boundary value problem," *Ann. Math.*, vol. 143, pp. 71–96, 1996.

[38] A. I. Nachman and M. J. Ablowitz, "A multi-dimensional inverse scattering method," *Studies Appl. Math.*, vol. 71, pp. 243–250, 1984.

[39] R. G. Novikov, "Multidimensional inverse spectral problem for the equation $-\mathrm{Delta}\psi + (\nu(x) - Eu(x))\psi = 0$," *Funktsional. Anal. i Ego Prilozhen*, vol. 22, pp. 11–22, 1988. (Transl. *Funct. Anal. and Applicat.* vol. 22, pp. 263–272, 1988,).

[40] ——, "The inverse scattering problem on a fixed energy level for the two-dimensional Schrödinger operator," *J. Funct. Anal.*, vol. 103, pp. 409–463, 1992.

[41] R. G. Novikov and G. M. Khenkin, "The $\bar{\partial}$-equation in the multidimensional inverse scattering problem," *Uspekhi Mat. Nauk.*, vol. 42, pp. 93–152, 1987.

[42] F. Santosa and M. Vogelius, "A backprojection algorithm for electrical impedance imaging," in *SIAM J. Appl. Math.*, vol. 50, 1990, pp. 216–243.

[43] S. Siltanen, J. Mueller, and D. Isaacson, "An implementation of the reconstruction algorithm of A. Nachman for the 2-D inverse conductivity problem," *Inverse Problems*, vol. 16, pp. 681–699, 2000.

[44] ——, "Errata: An implementation of the reconstruction algorithm of A. Nachman for the 2-D inverse conductivity problem," *Inverse Problems*, vol. 17, pp. 1561–1563, 2001.

[45] S. Siltanen, J. Mueller, and D. Isaacson *et al.*, "Reconstruction of high contrast 2-D conductivites by the algorithm of A. Nachman," in *Proc. 2000 Conf. Radon Transforms and Tomography*, E. T. Quinto *et al.*, Eds., 2001, pp. 241–254.

[46] S. J. Simske, *An Adaptive Current Determination and a One-Step Reconstruction Technique for a Current Tomography System*. Troy, NY: RensselaerPolytech. Inst., 1987.

[47] E. Somersalo, M. Cheney, D. Isaacson, and E. Isaacson, "Layer stripping: A direct numerical method for impedance imaging," *Inverse Problems*, vol. 7, pp. 899–926, 1991.

[48] E. Somersalo, M. Cheney, and D. Isaacson, "Existence and uniqueness for electrode models for electric current computed tomography," in *SIAM J. Appl. Math.*, vol. 52, 1992, pp. 1023–1040.

[49] A. J. Suroviec, S. S. Stuchly, J. R. Barr, and A. Swarup, "Dielectric properties of breast carcinoma and the surrounding tissues," *IEEE Trans. Biomed. Eng.*, vol. 35, pp. 257–263, Apr. 1988.

[50] A. Swarup, S. S. Stuchly, and A. Surowiec, "Dielectric properties of mouse mca1 fibrosarcoma at different stages of development," *Bioelectromagnetics*, vol. 12, no. 1, p. 108, 1991.

[51] J. Sylvester, "A convergent layer stripping algorithm for the radially symmetric impedance tomography problem," *Commun. Partial Differential Equations*, vol. 17, pp. 1955–1994, 1992.

[52] A. Wexler, B. Fry, and M. Neuman, "Impedance computed tomography algorithm and system," *Appl Opt.*, vol. 24, pp. 3982–3985, 1985.

[53] T. J. Yorkey, J. G. Webster, and W. J. Tompkins, "Comparing reconstruction algorithms for electrical impedance tomography," *IEEE Trans. Biomed. Eng.*, vol. BME-34, pp. 843–852, 1987.